RESEARCH ARTICLE

ADVANCED MATERIALS
www.advmat.de

Mechanochemically Robust $LiCoO_2$ with Ultrahigh Capacity and Prolonged Cyclability

Weiyuan Huang, Jianyuan Li, Qinghe Zhao, Shunning Li, Mingyuan Ge, Jianjun Fang, Zhefeng Chen, Lei Yu, Xiaozhou Huang, Wenguang Zhao, Xiaojing Huang, Guoxi Ren, Nian Zhang, Lunhua He, Jianguo Wen, Wanli Yang, Mingjian Zhang, Tongchao Liu,* Khalil Amine,* and Feng Pan**

Pushing intercalation-type cathode materials to their theoretical capacity often suffers from fragile Li-deficient frameworks and severe lattice strain, leading to mechanical failure issues within the crystal structure and fast capacity fading. This is particularly pronounced in layered oxide cathodes because the intrinsic nature of their structures is susceptible to structural degradation with excessive Li extraction, which remains unsolved yet despite attempts involving elemental doping and surface coating strategies. Herein, a mechanochemical strengthening strategy is developed through a gradient disordering structure to address these challenges and push the $LiCoO_2$ (LCO) layered cathode approaching the capacity limit (256 mAh g^{-1}, up to 93% of Li utilization). This innovative approach also demonstrates exceptional cyclability and rate capability, as validated in practical Ah-level pouch full cells, surpassing the current performance benchmarks. Comprehensive characterizations with multiscale X-ray, electron diffraction, and imaging techniques unveil that the gradient disordering structure notably diminishes the anisotropic lattice strain and exhibits high fatigue resistance, even under extreme delithiation states and harsh operating voltages. Consequently, this designed LCO cathode impedes the growth and propagation of particle cracks, and mitigates irreversible phase transitions. This work sheds light on promising directions toward next-generation high-energy-density battery materials through structural chemistry design.

1. Introduction

Lithium-ion batteries serve as the ubiquitous power supplier in portable electronics, power tools, and the ever-expanding electric vehicle market.[1–3] While the pursuit of theoretical capacity has proven effective in improving energy density, this success has been predominantly observed in the case of the low-energy-density $LiFePO_4$ cathode where complete removal of Li^+ ions barely affects its structure framework. However, critical challenges emerge when attempting to approach the theoretical capacity of layered oxide cathodes, which exhibit the highest energy density among commercial cathodes. These cathodes feature a structure composed of alternately-stacked lithium (Li) and transition metal (TM) layers within the oxygen framework, rendering them sensitive to the extent of Li removal.[4,5] As more Li^+ ions are extracted out of the lattice, such structure becomes susceptible to irreversible TM migration and the instability of the anionic framework, accompanied with detrimental phase transformations and oxygen release.[6,7] Therefore,

---

W. Huang, J. Li, Q. Zhao, S. Li, J. Fang, Z. Chen, W. Zhao, F. Pan
School of Advanced Materials
Peking University Shenzhen Graduate School
Shenzhen 518055, China
E-mail: panfeng@pkusz.edu.cn

W. Huang, X. Huang, T. Liu, K. Amine
Chemical Sciences and Engineering Division
Argonne National Laboratory
Lemont, IL 60439, USA
E-mail: liut@anl.gov; amine@anl.gov

M. Ge, X. Huang
National Synchrotron Light Source II (NSLS-II)
Brookhaven National Laboratory
Upton, NY 11973, USA

The ORCID identification number(s) for the author(s) of this article can be found under https://doi.org/10.1002/adma.202405519

DOI: 10.1002/adma.202405519

L. Yu, J. Wen
Center for Nanoscale Materials
Argonne National Laboratory
Lemont, IL 60439, USA

G. Ren, N. Zhang
State Key Laboratory of Functional Materials for Informatics
Shanghai Institute of Microsystem and Information Technology
Chinese Academy of Sciences
Shanghai 200050, China

L. He
Beijing National Laboratory for Condensed Matter Physics
Institute of Physics
Chinese Academy of Sciences
Beijing 100190, China

W. Yang
Advanced Light Source
Lawrence Berkeley National Laboratory
Berkeley, CA 94720, USA

it has been long believed that only ≈50–60% of Li (corresponding to the capacity of 140–165 mAh g^{-1}) can be reversibly extracted from a layered structure like LCO.[8,9]

Increasing the upper operating voltage stands as the most direct method to drive LCO cathodes toward their theoretical specific capacity limit. Recent efforts, such as elemental doping[10,11] and surface coating,[12,13] demonstrate some potential in enhancing bulk and surface structural stability, elevating the operating voltage to 4.5 and 4.6 V, thereby enabling Li utilization up to 70–80% (equivalent to 190–220 mAh g^{-1}). Surface spinel-like structures [14,15] and high-entropy structure design[16] also gained great attention as effective approaches in inhibiting the undesired interfacial side reactions and restraining detrimental surface phase transition. Some reports even push the operating voltage of LCO to 4.7 and 4.8 V. However, despite these elevated voltages, the effective operating voltage was consistently constrained to ≈4.6 V due to increased overpotential, as evidenced by the restricted Li utilization of 80–85% (equivalent to 220–230 mAh g^{-1}).[17–19] Moreover, the higher capacity comes at the cost of rapid electrochemical decay within limited cycles.[20,21] Up to the present, nearly all the reported layered cathodes still suffer from significant anisotropic lattice variation and strain, leading to mechanical fatigue and particle microcracks upon repeated cycles, particularly under high delithiation states.[22–26] The formation of microcracks exposes fresh surfaces to the electrolyte, triggering severe interfacial parasitic reactions and detrimental phase transitions, thus accelerating electrochemical degradation.[27–29] Therefore, despite the potential for a capacity improvement of 60–70 mAh g^{-1} toward theoretical capacity, achieving higher Li utilization in commercial applications remains a formidable challenge because the mechanical fatigue imposed by their intrinsic structural nature has yet to be resolved.

Herein, depicted in **Figure** 1a, we introduce an innovative gradient disordering structure design for LCO cathodes (referred to as GDLCO), which establishes a new benchmark performance by fundamentally mitigating the mechanical fatigue of the layered framework. The gradient disordering structure is composed of an outmost surface with significant disordering, a subsurface with partial disordering, and the bulk with tiny disordering. The highly disordered structure at the outermost surface forms a rock-salt phase that is structurally coherent with the layered structure but electrochemically much more stable, securing an ultra-wide operating voltage window of 1.5–5.0 V.[30,31] Benefitting from the atomic disordering within the framework, GDLCO presents a larger energy increase with the lattice contraction and expansion (Figure 1b; Figure S1, Supporting Information), indicating a high resistance against lattice strain. Its excellent cyclability and rate capability are confirmed by electrochemical evaluations at various scales, including Ah-level pouch full cells. This work clearly demonstrates that solving lattice strain and mechanical fatigue can address the longstanding trade-off between capacity and stability, which opens a new avenue for cathode material development.

2. Results and Discussion

2.1. Mechanochemically Robust Structure Design

To achieve the desired structure, the material was carefully prepared through high-temperature solid-state calcination, followed by a solution process and moderate-temperature calcination in an inert atmosphere (refer to the experimental section for details). X-ray diffraction (XRD) pattern can be indexed to the typical layered structure with space group $R\text{-}3m$ (Figure 1c), similar to pristine LCO (Figure S2, Supporting Information). Rietveld refinement reveals ≈2.0% Co cations residue in the Li layer (Tables S1,S2, Supporting Information). The SEM image shows the single crystalline particle morphology with sizes ranging from 3 to 5 µm (Figure S3, Supporting Information). The continuous rotation electron diffraction (cRED) results of GDLCO (Figure S4, Supporting Information) exhibit discrete and clear reflections along the c^* and (210) directions, revealing the single-crystal nature of individual particles with a well-defined layered structure. The atomic structures from the surface to the bulk were investigated by atomic-resolved spherical aberration-corrected scanning transmission electron microscopy (STEM). As shown in Figure 1d, the outmost surface exhibits a disordered rock-salt phase, and then gradually transits into a disordered layered phase and an ordered layered phase with the depth, showing a gradient of disordering decrease from surface to bulk. Notably, Li/Co disordering persists within the bulk-ordered layered structure, highlighted by the arrows. The corresponding fast Fourier transform (FFT) maps further confirm the gradient structural configuration of GDLCO, which illustrates the transition from the outermost rock-salt structure (Figure 1e) toward disordered layered (a combination of layered and rock-salt, indicated by circled rock-salt diffraction spots in Figure 1f) and eventually to the bulk layered structure with limited Li/Co disordering (Figure 1g). Energy dispersive spectroscopy (EDS) mapping shows Al and F elemental distribution at the particle surface (Figure S5, Supporting Information). The Al: Co molar ratio was determined to be 0.001: 0.999 by ICP-OES (Table S3, Supporting Information). Subsequent investigation into the distribution of Al and F elements within the cross-section sample through EDS line scan characterization indicated an enrichment of Al and F at the particle surface, with respective thicknesses of ≈10 and 7 nm (Figure S6, Supporting Information). The outermost molar ratio of F: O was ≈0.86: 1.14, while the molar ratio of Al: Co shows the highest value of 0.28: 0.72 at a depth of ≈4 nm near the surface region. Al and F penetration induces the formation of a well-defined rock-salt surface structure, distinct from LCO after direct calcination, which exhibits a defected spinel-like surface (Figure S7, Supporting Information). The effects of secondary calcination and elemental diffusion gradually decrease from surface to bulk, leading to a special rock-salt to disordering and ordering gradient structure in the desired material. The high bonding energy of Al—O and Co—F, coupled with the presence of lower Co valence states (Figure S8, Supporting Information), are anticipated to stabilize the surface structure and alleviate surface side reactions.[32,33]

M. Zhang
School of Science and Engineering
The Chinese University of Hong Kong
Shenzhen 518172, China
E-mail: zhangmingjian@cuhk.edu.cn

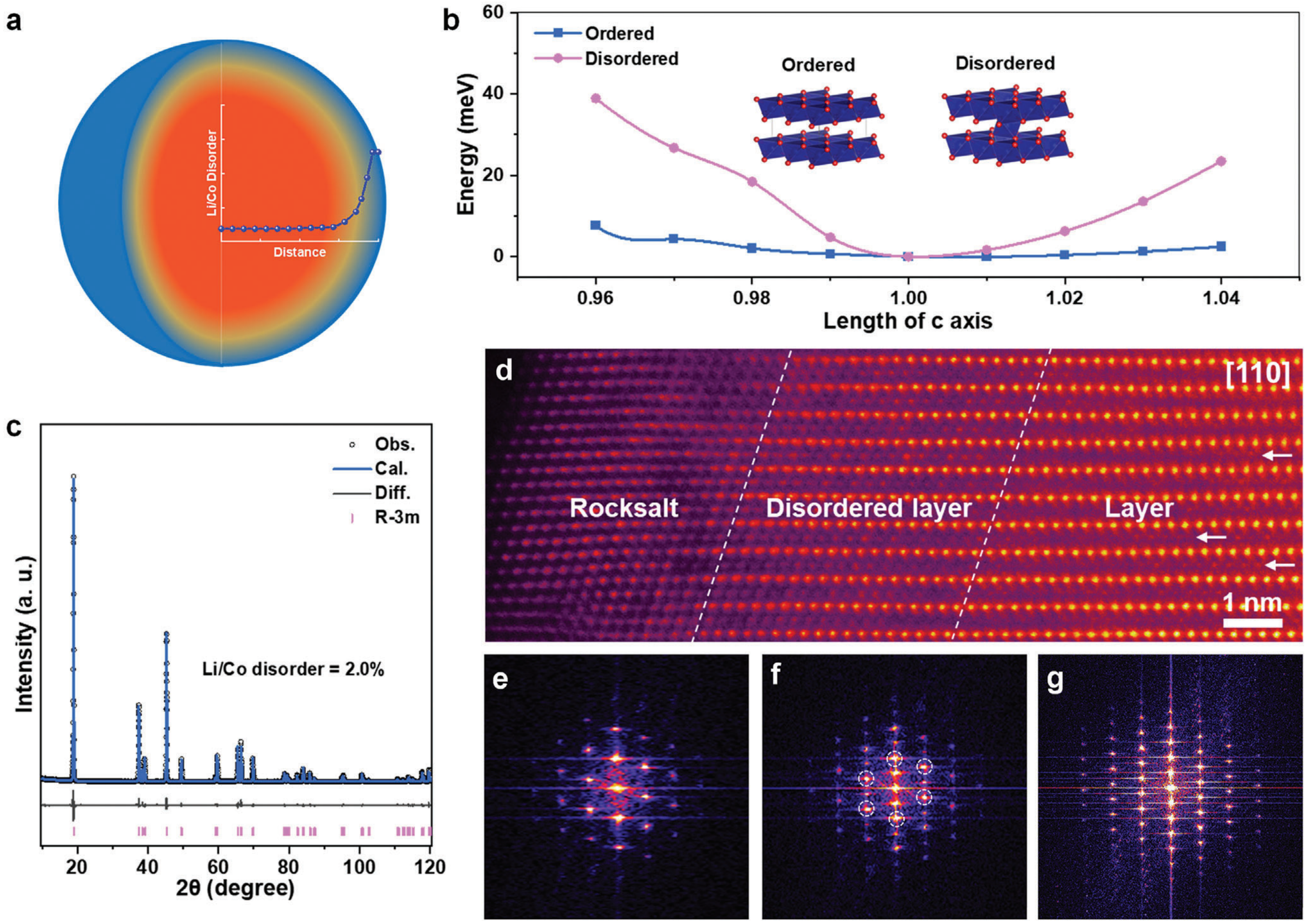

Figure 1. a) Schematic diagram of the GDLCO particle with gradient Li/Co disorder structure. The extent of disordering decreases from surface to bulk. b) The calculated energy as a function of the strain along the *c* axis for ordered and disordered samples at fully delithiated states. c) XRD pattern and Rietveld refinement result of GDLCO cathode. d) High-resolution TEM image with atomic resolution of GDLCO. e–g) FFT maps deduced from surface to bulk regions in (d).

2.2. Electrochemical Performance

The electrochemical performance of GDLCO and LCO was evaluated in both coin half cells and pouch full cells. The carbonate electrolyte employed in this work can stabilize up to 4.7 V (Figure S9, Supporting Information). **Figure** 2a shows the initial discharge capacities of 256 and 251 mAh g^{-1} for GDLCO and LCO, respectively, at 0.1 C (1 C = 200 mA g^{-1}) in 3–4.65 V, ≈93% of the theoretical capacity. The dQ/dV curves delineate the phase transition behaviors observed in the initial two cycles (Figure S10, Supporting Information). The extra capacity of ≈30 mAh g^{-1} was derived from the charged plateau of 4.62 V, signifying the transition from the H1-3 to O1 phase.[8] This capacity plateau tends to be absent in most reported cathodes even when charged to higher operating voltages, primarily due to their sluggish kinetics.[14,16] The extended cycling tests demonstrate the exceptional performance of GDLCO, presenting a remarkable capacity retention of 82% after 500 cycles at 5 C and an average voltage decay of only 0.048 V (0.096 mV per cycle) (Figure 2b; Figure S11, Supporting Information). This stands in stark contrast to pristine LCO, which shows a capacity retention of only 42% and an average voltage decay of 0.557 V (1.114 mV per cycle). Correspondingly, the substantial peak intensity decrease and peak position shift with cycling in the dQ/dV profiles indicate that LCO undergoes serious irreversible structural evolution and electrochemical decay (Figure S12, Supporting Information). When cycled at 1 C, a high capacity of 245 mAh g^{-1} can be achieved with 89% capacity retention after 100 cycles (Figure S13, Supporting Information). Furthermore, by limiting the upper cutoff voltage to 4.6 V, the cycling stability of GDLCO is further enhanced. It achieves an 82% retention and a minimal average voltage decay of 0.136 V (0.091 mV per cycle) after an impressive 1500 cycles at 10 C (Figure 2c). In contrast, the discharged capacity of LCO rapidly declines to nearly zero, experiencing a large voltage decay of 0.804 V (2.68 mV per cycle) after only 300 cycles at 10 C.

The cycling stability of GDLCO was further examined in pouch full cells. The cell shows an initial capacity of 841 mAh with a capacity retention of 81% after 300 cycles when cycled at 3–4.6 V (equivalent 4.65 V vs Li/Li^+ in the half cell) at 0.75 C (Figure 2d). To validate the practicability of the pouch full cells, we assembled 6 pouch cells in series as a pack (≈2 Ah for each single pouch cell, a total of 12 Ah) to power a high-speed drone that requires

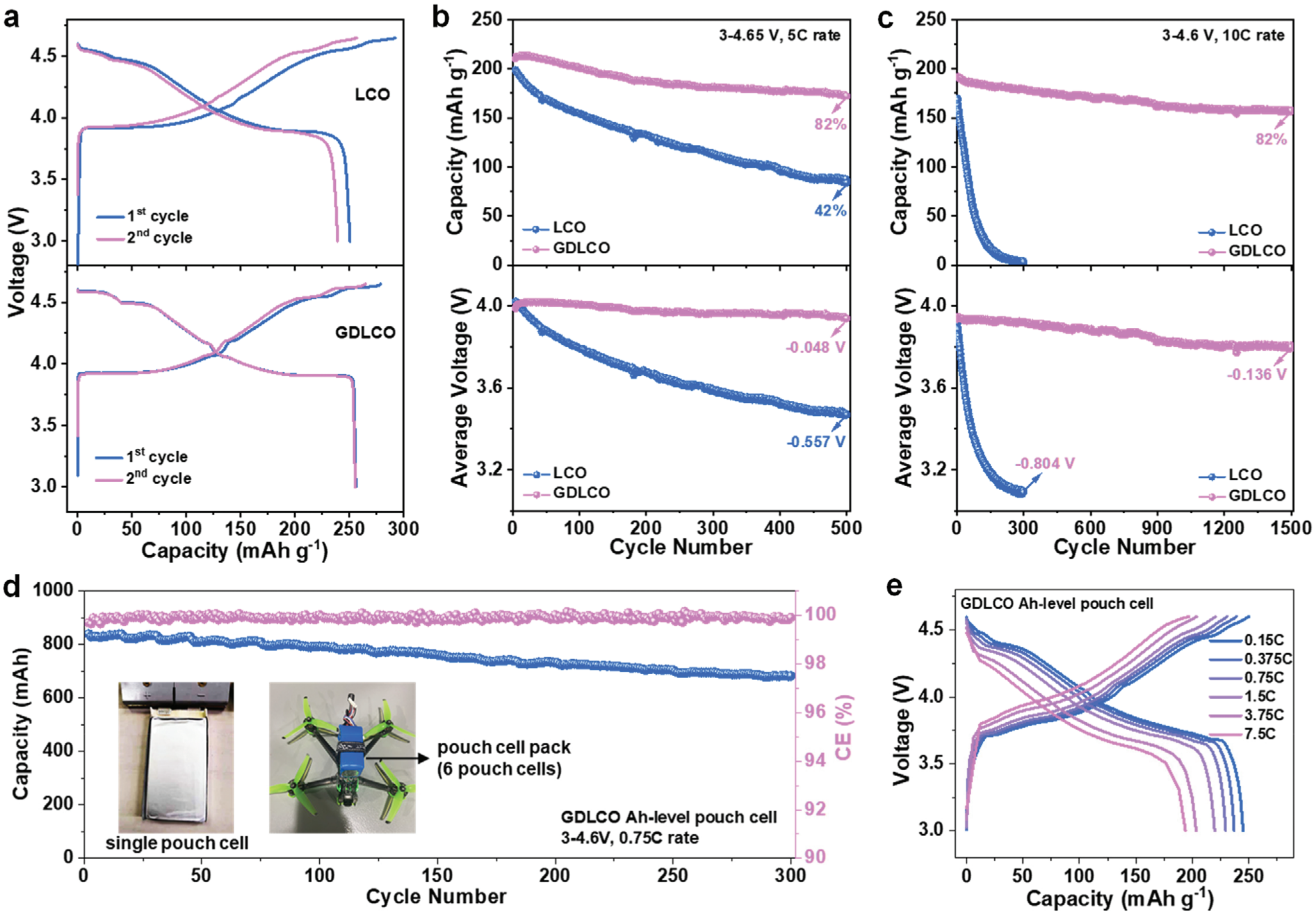

Figure 2. a) The initial two cycles charge/discharge profiles of LCO and GDLCO cathodes within 3–4.65 V under 0.1 C. b) The capacity and average voltage stability of LCO and GDLCO half cells within 3–4.65 V under 5 C. c) The capacity and average voltage stability of LCO and GDLCO half cells within 3–4.6 V under 10 C. d) The cyclic stability of the Ah-level pouch full cell within 3–4.6 V (equal to 4.65 V vs Li/Li$^+$) under 0.75 C. Inset: the single pouch cell and pouch cell pack powering the unmanned aerial vehicle. e) The rate performance of the pouch cell from 0.15 to 7.5 C.

high power density batteries (inset of Figure 2d, the flight tests provided in Video S1, Supporting Information). The pouch full cell exhibits a discharge capacity of 250 mAh g^{-1} at 0.15 C and keeps 195 mA h g^{-1} at 7.5 C (Figure 2e). To further evaluate the high rate capability of GDLCO, three pouch full cells were first charged at the same rate of 3.75 C, and then discharged at 7.5 C, 15 C, and 30 C, respectively (Figure S14, Supporting Information). Surprisingly, nearly identical discharge capacities of ≈204 mAh g^{-1} were achieved consistently from 7.5 C to 30 C. This achievement marks the first instance of attaining such high capacity at extremely high current rates in practical pouch full cells. Compared to GDLCO, LCO demonstrates a fast capacity decline when current rates increase (Figure S15, Supporting Information). This suggests that a robust structure framework serves as a fundamental requirement for facilitating rapid Li$^+$ extraction and insertion, emphasizing its significance for enabling fast charging capabilities. The electrochemical tests underscore the great success of the gradient disordering structure design on GDLCO cathodes, particularly in challenging operational conditions like extended cycling and fast charging/discharging, which outperforms all previous LCO cathodes (Table S4, Supporting Information).

2.3. Mechanism Exploration of the Structural Stability

To gain a comprehensive understanding of the positive effects on the electrochemical properties stemming from the gradient disordering structure design, our study extensively delved into the chemical, mechanical, and atomic structural evolutions of the materials across multiple scales. We utilized full-field transmission X-ray microscopy (TXM) in conjunction with 3D X-ray absorption near-edge spectroscopy (XANES) to investigate the electrode chemistry at various charge states. **Figure 3a–c** presents the 3D rendering of the Co valence distribution of GDLCO at open-circuit voltage (OCV), charged to 4.6 and 4.65 V, respectively. The color changes from blue to green, then to yellow and red, demonstrating the gradual oxidation process of Co cations. By inspecting the color, we observed an obvious increase in an oxidation state of Co from OCV to 4.6 V, but less difference between 4.6 and 4.65 V. Similar observation is further confirmed by the 2D slice and cross-section views (Figure 3e–g; Figure S16, Supporting Information). For comparison, the corresponding 3D rendering and 2D slice view of LCO charged to 4.65 V were displayed in Figure 3d,h. In Figure 3i, we counted over all the voxels in the 3D XANES to quantify the changes in the valence state of Co. There

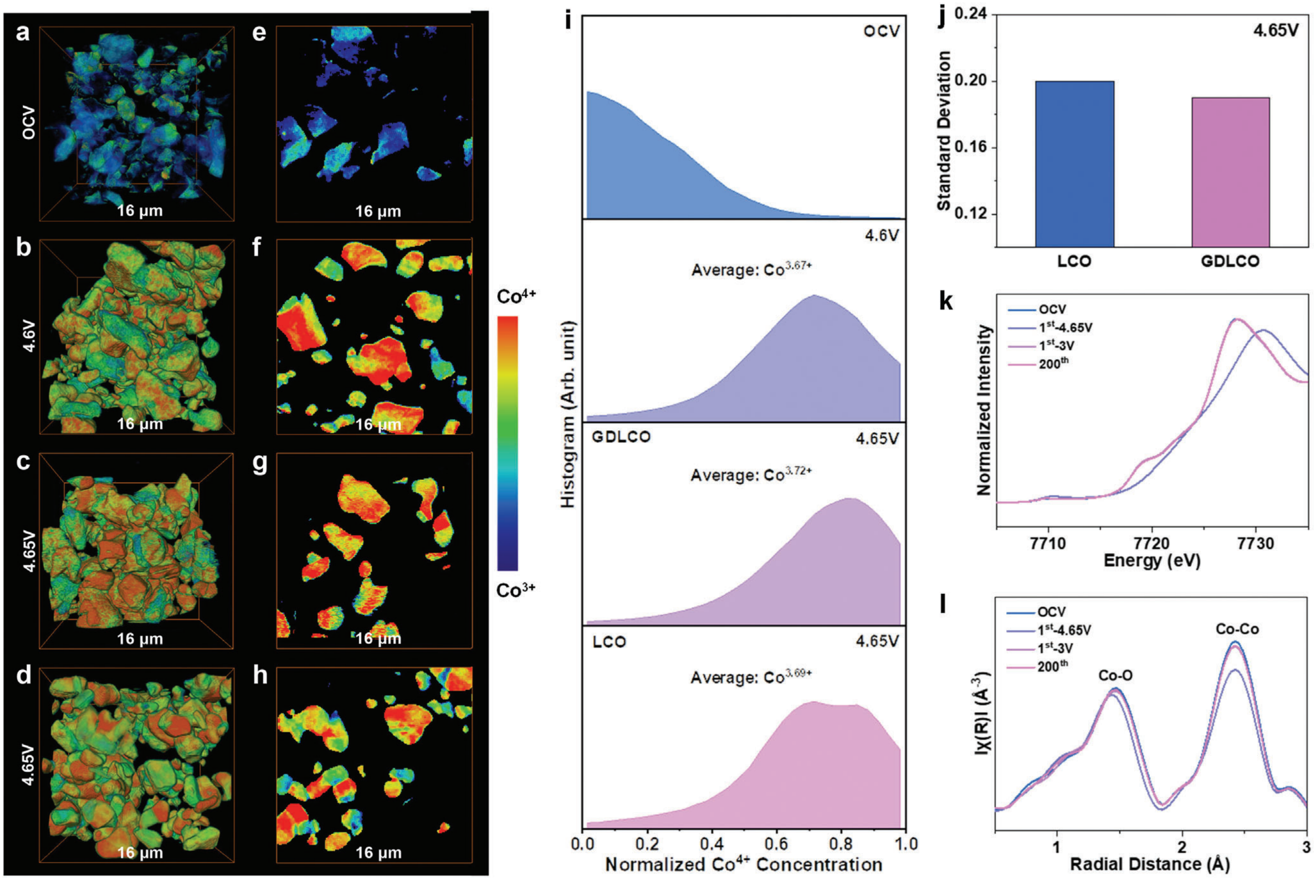

Figure 3. a–f) The 3D rendering (a–c) and 2D slice views (e–g) of Co valence distribution for GDLCO samples at OCV state, charged to 4.6 and 4.65 V by TXM technique. d,h) The 3D rendering (d) and 2D slice view (h) of Co valence distribution for LCO charged to 4.65 V. i) The corresponding Co valence state distribution curves of LCO and GDLCO. j) The standard deviation values of Co valence state distribution for LCO and GDLCO charged to 4.65 V. k,l) Co K-edge XANES (k) and EXAFS (l) spectra of GDLCO at OCV state, charged to 4.65 V, discharged to 3 V and after 200 cycles.

is an increase of 0.05 in Co average valence from 4.6 V (+3.67) to 4.65 V (+3.72) for GDLCO, corresponding to a capacity of only 13.7 mA h g^{-1}. The additional capacity is likely attributed to contributions from anionic redox occurring within the bulk above 4.6 V (Figure S17, Supporting Information), which was reported in many previous literatures.[34,35] Detailed evaluation of the particles enables the analysis of Co valence state distribution, both among particles and within individual ones of LCO and GDLCO. To quantify the chemical inhomogeneity, we introduced the standard deviation parameter derived from the voxel count in 3D XANES. A lower standard deviation value observed in GDLCO indicates enhanced chemical reaction homogeneity (Figure 3j). As indicated by the in situ XRD, LCO cathodes undergo significant lattice changes, particularly at high delithiation states. This observation suggests that the inhomogeneous reactions occurring at higher voltages could be more detrimental, as they result in a broader lattice parameter distribution and strain accumulation within single particles. Further investigations of the Co chemical states and local coordination environment transitions of GDLCO were conducted using X-ray absorption spectroscopy. The Co XANES curves distinctly display a positive shift in the white line when charged from OCV to 4.65 V, whereas no noticeable shift in curve position or change in shape occurred after 200 cycles (Figure 3k). Correspondingly, the Fourier-transformed extended X-ray absorption fine structures (EXAFS) show negligible changes in the Co–O and Co–Co coordination distances after long-term cycling, implying a stable local coordination environment for GDLCO (Figure 3l).

The reversible structural evolution during cycling plays a pivotal role in ensuring long-term stability. Consequently, in situ, high-energy XRD measurements were performed to examine the structural reversibility during the charge–discharge process. As shown in **Figure** 4a,b and Figures S18,S19 (Supporting Information), both LCO and GDLCO shows obvious structural evolution with most diffraction peaks shifting during delithiation/lithiation process. Initially, the (003) and (104) peaks shift toward lower angles, indicating expansion in interlayer spacing due to the increased electrostatic repulsion with Li$^+$ extraction. Upon reaching minimum 2θ at 4.25 V, the peaks significantly shift toward higher angles, suggesting a rapid reduction in interlayer spacing concurrently with the successive phase transitions. During the discharge process, all the diffraction peaks revert to original positions, signifying the reversal of the phase transition process. Notably, GDLCO experiences highly reversible phase transitions in the second cycle, exhibiting the same phase transition at high delithiation states. In contrast, LCO has suffered from

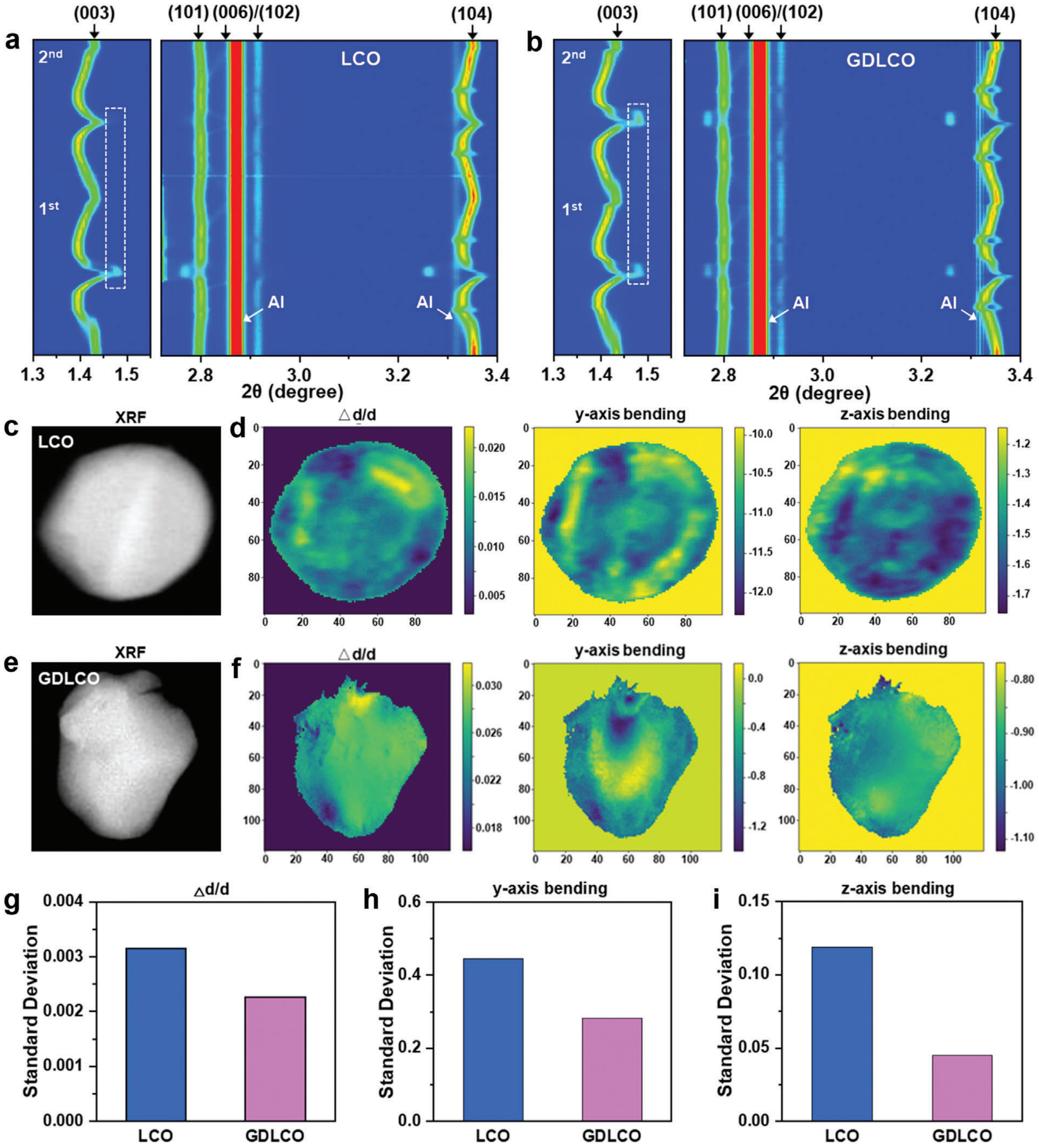

Figure 4. a,b) In situ XRD contour plots of LCO and GDLCO in the initial two cycles. c,e) The XRF images illustrate the morphology of LCO (c) and GDLCO (e). d,f) Spatial visualizations show three distinct lattice dislocations: lattice expansion/contraction $\triangle d/d$, *y*-axis, and *z*-axis slab bending along (101) plane of LCO (d) and GDLCO (f) charged to 4.65 V. g–i) The comparison of standard deviation values of $\triangle d/d$ (g), *y*-axis (h), and *z*-axis (i) slab bending along (101) plane.

subtle structural degradation during the initial cycle (highlighted by the dashed rectangle). which impeded the delithiation process at high operating voltages in subsequent cycles. From this, it can be inferred that the gradient disordering structure demonstrates a stable lattice framework for persistent Li^+ diffusion. To monitor the structure evolution process of both the cathode and anode materials under practical operating conditions, in situ, neutron diffraction measurement was carried out in a GDLCO Ah-level pouch full cell. As shown in Figure S20 (Supporting Information), the pouch cell exhibits similar charge plateaus at 4.50 and 4.58 V (equivalent to 4.55 and 4.63 V in the half cell). With the charge plateau at 4.58 V (marked by the dashed horizontal line), the phase transition from H1-3 to O1 is clearly identified, as evidenced by the shift of the (104) peak. The structure reversibly transforms back to the H1-3 phase with the corresponding discharge plateau at 4.44 V. In addition, the reversible phase transition from graphitized C to LiC_{12} and LiC_6 on the graphite anode is also observed, indicating the interaction between GDLCO cathode and graphite anode.

Scanning diffraction X-ray microscopy (SDXM) serves as a powerful technique for directly observing lattice dislocations and strain evolution within individual particles, enabling the assessment of subtle structural changes in LCO and GDLCO cathodes when charged to 4.65 V. As depicted in Figure 4c,e, X-ray fluorescence (XRF) images show the morphology of the selected particles. Additionally, the diffraction-contrast sum images were presented in Figure S21 (Supporting Information). The spatial visualizations present three distinct lattice distortions: lattice expansion/contraction $\Delta d/d$, y-axis slab bending, and z-axis slab bending. Lattice expansion/contraction $\Delta d/d$ is characterized by variations in the momentum transfer magnitude, detected by measuring changes in the total scattering angle 2θ. As for the 2θ value to remain unchanged and the momentum transfer rotates to a different orientation, such as along the y- or z-axis, a phenomenon termed y- or z-axis slab bending. In Figure 4d,f, the blue and yellow colors respectively represent lattice dislocations either along or opposite to the (101) peak direction from the standard crystal lattice. GDLCO exhibits reduced lattice variations of $\Delta d/d$, y-axis, and z-axis bending at ≈0.012, 1.2, and 0.3, respectively. These values are notably lower than those of LCO, which measure 0.015, 2.0, and 0.5 for the same parameters. Correspondingly, the standard deviation values of GDLCO were determined to be 0.0023, 0.28, and 0.045, respectively, which are lower than those of LCO at 0.0032, 0.45, and 0.12 (Figure 4g–i). The above results clearly prove the gradient disordering structure design can effectively mitigate lattice dislocation and strain generation, and contributes to the enhanced structural reversibility and stability at both the particle and electrode levels.

The morphology and local structure stability indeed wield significant influence on the electrochemical performance of the cathodes. As depicted in **Figures** 5a and S22a (Supporting Information), high-resolution TEM images exhibit severe particle cracking occurring both on the surface and within LCO particles upon charging to 4.65 V. This cracking coincides with a phase transition to a spinel-like structure and pronounced lattice distortion. This phenomenon is further validated by streak reflections along the c^*-axis in the corresponding cRED map (Figure 5j, with a schematic illustration of the cRED technique shown in Figure 5i). The substantial structural distortion and the emergence of nano-cracks at 4.65 V can be attributed to significant and inhomogeneous changes in interlayer spacing accompanying the detrimental phase transitions. The generation of microcracks significantly intensifies side reactions at the electrolyte-particle interface (Figure S23, Supporting Information), hastening the electrochemical degradation. In stark contrast, GDLCO maintains its layered structure with minimal lattice distortion even at high charging voltages (Figure 5e,m; Figure S22b, Supporting Information). Upon discharging back to 3.0 V, both the diffraction patterns in the FFT map derived from the high-resolution TEM image (Figure 5f) and the cRED pattern (Figure 3n) for GDLCO exhibit a complete recovery of sharpness. This suggests a restoration of lattice distortion after discharge. As for LCO, the lattice distortion persists around the nano-crack regions after discharge (Figure 5b,k). It's intriguing that within these cracks, partial lattice fringes are visible when charged to 4.65 V or discharged to 3 V in the initial cycles. This suggests that the cracks formed during these early cycles of LCO might resemble pseudo-cracks, indicating a behavior akin to phase segregation triggered by local structural transitions. More importantly, the layered structure remains intact and well-maintained in GDLCO even after 200 cycles (Figure 5g,h,o), while LCO cathodes show severe lattice distortion (Figure 5l), significant corrosion and crack formation (Figure 5c,d). The TEM and corresponding FFT analysis verify the presence of rock-salt and spinel-like phases surrounding the cracks in the cycled LCO (Figure 5d). The structural damages induced by chemo-mechanical fatigue can block effective pathways for Li^+ diffusion, leading to rapid capacity decay. In contrast, gradient-disordered structures exhibit greater resistance to mechanical degradation and ensure structural integrity. This, in turn, facilitates persistent Li^+ diffusion even under harsh operating voltages and extended cycling conditions.

3. Conclusion

In summary, a practical gradient disordering structure design strategy was developed to address the long-standing challenge of mechanochemical failure in layered cathodes. The resulting GDLCO cathodes demonstrate robust resistance to chemo-mechanical strains, effectively suppressing microcrack formation, minimizing surface side reactions, and mitigating irreversible phase transformations even under high voltages. Consequently, GDLCO achieves an exceptionally high practical reversible capacity, pushing Li utilization in layered oxide cathodes to 93% (256 mAh g^{-1}), while exhibiting enhanced cycling stability surpassing existing high-voltage cathode materials. We emphasize that such an unprecedented performance is achieved differing from hitherto elemental doping and surface coating strategies. In addition, it should be pointed out that a stable layered framework not only enhances cyclability but also provides persistent Li^+ diffusion pathways essential for high-rate capability especially under extreme operating conditions—an aspect often overlooked in prior investigations. This breakthrough unfolds the promising future in battery chemistry, paving the way for expanded research horizons dedicated to developing practical, high-performance cathode materials.

4. Experimental Section

Material Synthesis: The conventional LCO cathode was synthesized through solid-state calcination. Li_2CO_3 (99.5%, Aladdin) and CoO (99.5%, Aladdin) were meticulously mixed in a molar ratio of Li: Co = 1.03: 1 with a 3% Li excess in a pot mill for 20 h. Subsequently, the mixture was calcined in a muffle furnace at 900 °C for 12 h with a heating rate of 5 °C min^{-1}. The resulting product was thoroughly pulverized using a multi-function pulverizer.

For the gradient disordering structure of LCO, an initial step was dispersing 5 mol of LCO powders in 2 L of DI water in a 3L reactor under continuously stirring at a speed of 800 rpm. Then, 0.45 mol of $LiNO_3$ (99.5%, Aladdin) and 0.15 mol of $Al(NO_3)_3 \cdot 9H_2O$ (99%, Aladdin) were added to the reactor and continuously stirred until completely dissolved. Subsequently, 500 ml of 1.8 M NH_4F (99%, Aladdin) solution was pumped into the reactor at a speed rate of 5 ml min^{-1}. This mixture was continuously stirred at 80 °C for 5 h. After filtration to remove the solution, the

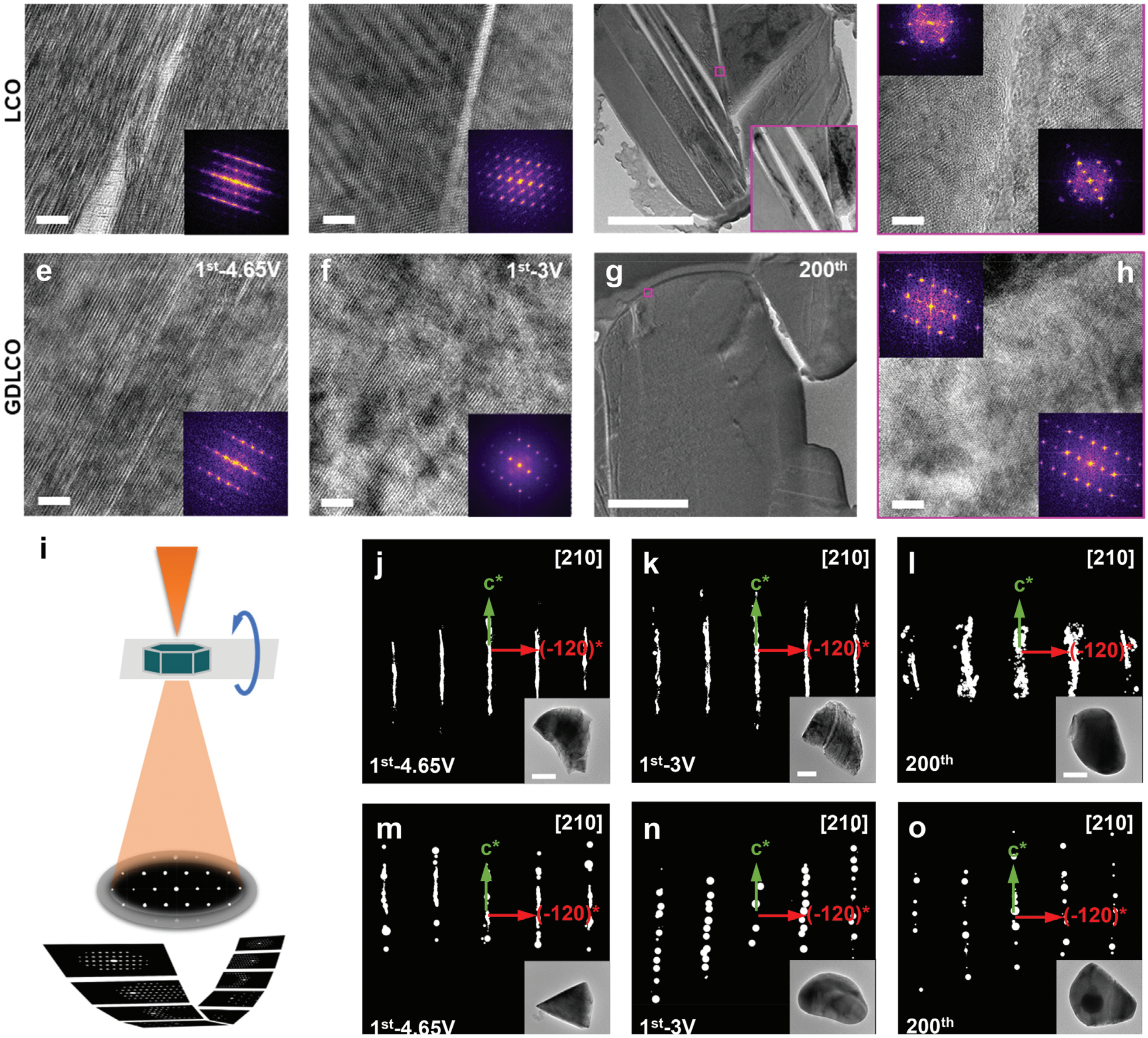

Figure 5. a–h) TEM images for LCO and GDLCO samples after the first charge to 4.65 V (a,e), the first discharge to 3 V (b,f), and after 200 cycles (c,d,g,h). The insets are the corresponding FFT maps. For (c), the inset shows the enlarged region of the cracks. The inset scalebar is 5 nm for (a,b,d–f,h) and 1 µm for (c,g). i, Schematic illustration of cRED technique. j–o) The reciprocal lattice pattern viewed along [210] direction for LCO and GDLCO particles after the first charge to 4.65 V (j,m), the first discharge to 3 V (k,n), and after 200 cycles (l,o). The inset is the selected particle for cRED with a scale bar of 500 nm.

product underwent drying at 80 °C for 6 h and subsequent calcination at 500 °C for 5 h in an Ar atmosphere to achieve the desired material.

Characterizations: The chemical composition was analyzed using inductively coupled plasma-optical emission spectroscopy (ICP-OES, Horiba Jobinyvon JY2000-2). The powder XRD measurement was performed on a Bruker D8 Advance diffractometer with a Cu-*Kα* radiation source. Rietveld refinements of the crystal structure were done using Fullprof software.[36] The morphology was observed by a field-emission scanning electron microscope (SEM, Carl Zeiss SUPRA@ 55). The transmission electron microscope (TEM) and cRED dataset were collected on a field-emission transmission electron microscope (FETEM, JEOL-3200FS) operating at an accelerating voltage of 300 kV with a 60 cm camera length, a minimum collection angle of −30° to 30°, and a OneView CMOS camera (Gatan Inc.). Atomic resolution TEM was conducted on Argonne Chromatic Aberration-Corrected TEM (ACAT) with an accelerating voltage of 200 kV.

Electrochemical Measurements: The LCO electrodes were prepared by mixing active material, conductive carbon black, and polyvinylidene difluoride (PVDF) binder at a weight ratio of 8: 1: 1 in *N*-methyl-2-pyrrolidone (NMP) solvent. The slurry was then cast onto an Al foil and dried at 120 °C overnight. The 2032 type coin half cells were assembled in an Ar-filled glovebox with cathode electrodes, lithium metal anodes, Celgard 2400 membrane, and 1 M $LiPF_6$ in EC/EMC (3: 7 in volume) electrolyte. The Ah-level pouch-type full cells with a capacity ratio of negative electrode capacity/positive electrode capacity (N/P ratio) 1.14:1 with a dimension of 5.6 cm × 3.3 cm were assembled using a pouch-cell production line. The negative electrode was fabricated with 92 wt% mesocarbon microbeads (MCMB) (99.5%, 330 mA h g^{-1}), 3 wt% Super P carbon black (99.5%, MTI corporation KJ GROUP) as a conductive additive, and 5 wt% Carboxymethyl Cellulose (CMC) as the binder. The positive electrode was fabricated with 92 wt% LCO as active material, 4 wt% CNT and 2 wt% acetylene black as conductive additive, and 2 wt% PVDF as the binder, with a high active loading of $\approx$22 mg cm^{-2}. The charge–discharge performance was carried out in the NEWARE battery test system. The homemade differential electrochemical mass spectrometry was applied to detect the gas evolution during the initial two cycles in real-time.

Full-field Transmission X-Ray Microscopy (TXM) Imaging: TXM at the FXI beamline (18-ID) at National Synchrotron Light Source II (NSLS-II) was used to generate a 3D nano-XANES dataset. Specifically, the 3D-XANES dataset was assembled from a collection of 3D tomography images taken at incident X-ray energies from 7.6 to 8.2 keV to analysis the Co valance states. At each energy, tomography was reconstructed from the projection images taken from 0–180° at 0.3° intervals, using the "gridrec" algorithm implemented in Tomopy, an open-source Python package.[37] The XANES spectra extracted from the OCV sample were used and charged to a 4.65 V sample as reference spectra. An in-house package pyXAS was used to perform the XANES curve fitting at each voxel.[38]

Soft X-Ray Absorption Spectroscopy (sXAS) Measurements: The soft X-ray absorption spectroscopy (sXAS) experiments were conducted at the Shanghai Synchrotron Radiation Facility (SSRF), under the storge ring conditions of 3.5 GeV and 220 mA current. The O *K*-edge sXAS spectra were measured at a bending magnet beamline 02B02 with photons energy range from 50 to 2000 eV of the SiP·ME2 platform. The photon flux was $\approx$1011 photons s^{-1} and the energy resolving power $E/\Delta E$ was up to 13 000@250 eV. The beam size at the sample was set to 150 µm × 50 µm. The spectra were collected using bulk-sensitive total fluorescence yield modes simultaneously at room temperature in an ultrahigh vacuum chamber.

In Situ High Energy XRD (HEXRD): In situ, HEXRD characterization was conducted during the charging and discharging processes at the 11-ID-C beamline of the Advanced Photon Source ($\lambda = 0.1173$ Å). The 2032-type coin cells used for testing were assembled with dual 3 mm holes in both the cathode and anode caps. Galvanostatic charging and discharging tests were performed using the MACCOR battery system.

In Situ Neutron Diffraction (ND): The in situ ND measurement of the prepared pouch-type full cell was conducted at General Purpose Powder Diffractometer, China Spallation Neutron Source. A 1.2 Ah pouch cell was used during the in situ experiment. Due to the limited beam time, the high current rate of C/3 was used when charged from OCV to 4.5 V and discharged below 4.4 V. The low current rate of C/10 was applied when charged above 4.5 V and discharged back to 4.4 V to study the structure reversibility at high operating voltages.

Scanning Diffraction X-Ray Microscopy (SDXM): X-rays (9 keV) were utilized, focused to approximately a 40 nm spot size using a Fresnel zone plate.[39] The scanning procedure involved moving the sample across this focused beam with 30 nm scanning steps and a 0.05-second dwell time. Simultaneous collection of fluorescence signals and Bragg diffraction patterns occurred at each scan position, using Vortex-ME3 and Merlin detectors, respectively. For SDXM measurements, the crystal underwent a rocking motion over a range of ±1°, with angular steps of 0.1° around the Bragg peak. At each rocking angle, a 2D raster scan was performed.

DFT Calculations: The calculations were performed using the plane-wave-based density functional theory (DFT) method as implemented in the Vienna ab initio simulation package.[40–43] The generalized gradient approximation (GGA) with the Perdew–Burke–Ernzerhof functional was chosen as the exchange-correlation potential. A cutoff energy was set as 520 eV and the electronic energy convergence criterion was set at 10^{-6} eV. The k-points of Brillouin zone integration were sampled with $6 \times 6 \times 6$ using the Γ-center scheme. In order to correctly characterize the localization of transition-metal *d*-electrons, the GGA+U method was used to account for the strong correlation in the calculations. The value of the Hubbard U parameter for Co was 3.3 eV.[44] Geometries were optimized until the forces on the atoms were less than 0.01 eV $Å^{-1}$. Spin-polarization was considered in all calculations, with a ferromagnetic ordering of Co atoms used as the initial configuration. To complement the deficiency of DFT in treating dispersion interactions, a van der Waals correction term developed by Grimme (D3) was adopted.[45] The relationship between *c*-axis length and the internal energy of transition metal oxides was explored by constructing a supercell with the *c*-axis increased and decreased by 1–4% and 1–4%, respectively.

Supporting Information

Supporting Information is available from the Wiley Online Library or from the author.

Acknowledgements

W.H., J.L., and Q.Z. contributed equally to this work. This work acknowledges and supported by the National Natural Science Foundation of China (52172175), National Key R&D Program of China (2021YFA1500600), the Basic and Applied Basic Research Foundation of Guangdong Province (No. 2021B1515130002), Soft Science Research Project of Guangdong Province (No. 2017B030301013), Shenzhen Science and Technology Research Grant (No. JCYJ20210324130812033 and ZDSYS201707281026184), International joint Research Center for Electric Vehicle Power Battery and Materials (No.2015B01015), Shenzhen Key Laboratory of New Energy Resources Genome Preparation and Testing (No. ZDSYS201707281026184), and Guangdong Key Laboratory of Design and calculation of New Energy Materials (No. 2017B030301013). This research used resources of the Advanced Photon Source (11-BM, 11-ID-C, and 26-ID-C), a U.S. Department of Energy (DOE) Office of Science User Facility operated by Argonne National Laboratory under Contract No. DE-AC02-06CH11357. Use of the National Synchrotron Light Source II (beamline 3-ID, 7-BM, and 18 ID) was supported by the US Department of Energy, an Office of Science user Facility operated by Brookhaven National Laboratory under contract number DE-SC0012704. This work was performed, in part, at the Center for Nanoscale Materials, an Office of Science user facility, supported by the U.S. Department of Energy, Office of Science, Office of Basic Energy Sciences, under Contract No. DE-AC02-06CH11357.

Conflict of Interest

The authors declare no conflict of interest.

Data Availability Statement

The data that support the findings of this study are available from the corresponding author upon reasonable request.

Keywords

fatigue resistance, gradient disordering, Li-ion battery cathode, prolonged cyclability, ultrahigh capacity

Received: April 18, 2024
Revised: May 16, 2024

---

[1] J. M. Tarascon, M. Armand, *Nature* **2001**, *414*, 359.
[2] D. Castelvecchi, E. Stoye, *Nature* **2019**, *574*, 308.
[3] S. Chu, Y. Cui, N. Liu, *Nat. Mater.* **2016**, *16*, 16.

[4] C. Delmas, C. Fouassier, P. Hagenmuller, *Phys. B+C* **1980**, *99*, 81.

[5] J. W. Choi, D. Aurbach, *Nat. Rev. Mater.* **2016**, *1*, 16013.

[6] T. Liu, L. Yu, J. Liu, J. Lu, X. Bi, A. Dai, M. Li, M. Li, Z. Hu, L. Ma, D. Luo, J. Zheng, T. Wu, Y. Ren, J. Wen, F. Pan, K. Amine, *Nat. Energy* **2021**, *6*, 277.

[7] P. Yan, J. Zheng, Z. Tang, A. Devaraj, G. Chen, K. Amine, J. Zhang, L. Liu, C. Wang, *Nat. Nanotechnol.* **2019**, *14*, 602.

[8] Y. C. Lyu, X. Wu, K. Wang, Z. Feng, T. Cheng, Y. Liu, M. Wang, R. Chen, L. Xu, J. Zhou, Y. Lu, B. Guo, *Adv. Energy Mater.* **2021**, *11*, 2000982.

[9] M. Li, J. Lu, Z. Chen, K. Amine, *Adv. Mater.* **2018**, *30*, 1800561.

[10] Q. Liu, X. Su, D. Lei, Y. Qin, J. Wen, F. Guo, Y. Wu, Y. Rong, R. Kou, X. Xiao, F. Aguesse, J. Bareño, Y. Ren, W. Lu, Y. Li, *Nat. Energy* **2018**, *3*, 936.

[11] J.-N. Zhang, Q. Li, C. Ouyang, X. Yu, M. Ge, X. Huang, E. Hu, C. Ma, S. Li, R. Xiao, W. Yang, Y. Chu, Y. Liu, H. Yu, X.-Q. Yang, X. Huang, L. Chen, H. Li, *Nat. Energy* **2019**, *4*, 594.

[12] K. Wu, P. Ran, B. Wang, F. Wang, J. Zhao, E. Zhao, *Adv. Sci.* **2024**, *11*, 2308258.

[13] S. Kalluri, M. Yoon, M. Jo, S. Park, S. Myeong, J. Kim, S. X. Dou, Z. P. Guo, J. Cho, *Adv. Energy Mater.* **2016**, *7*, 1601507.

[14] Y. He, X. Ding, T. Cheng, H. Cheng, M. Liu, Z. Feng, Y. Huang, M. Ge, Y. Lyu, B. Guo, *J. Energy Chem* **2023**, *77*, 553.

[15] W. Huang, Q. Zhao, M. Zhang, S. Xu, H. Xue, C. Zhu, J. Fang, W. Zhao, G. Ren, R. Qin, Q. Zhao, H. Chen, F. Pan, *Adv. Energy Mater.* **2022**, *12*, 2200813.

[16] X. Tan, Y. Zhang, S. Xu, P. Yang, T. Liu, D. Ma, J. Qiu, Z. Chen, Z. Lu, F. Pan, W. Chu, *Adv. Energy Mater.* **2023**, *13*, 2300147.

[17] X. Yang, C. Wang, P. Yan, T. Jiao, J. Hao, Y. Jiang, F. Ren, W. Zhang, J. Zheng, Y. Cheng, X. Wang, W. Yang, J. Zhu, S. Pan, M. Lin, L. Zeng, Z. Gong, J. Li, Y. Yang, *Adv. Energy Mater.* **2022**, *12*, 2200197.

[18] J.-G. Lee, B. Kim, J. Cho, Y.-W. Kim, B. Park, *J. Electrochem. Soc.* **2004**, *151*, A801.

[19] Z. Zhuang, J. Wang, K. Jia, G. Ji, J. Ma, Z. Han, Z. Piao, R. Gao, H. Ji, X. Zhong, G. Zhou, H. M. Cheng, *Adv. Mater.* **2023**, *35*, 2212059.

[20] A. T. Appapillai, A. N. Mansour, J. Cho, Y. Shao-Horn, *Chem. Mater.* **2007**, *19*, 5748.

[21] W. M. Seong, K. Yoon, M. H. Lee, S. K. Jung, K. Kang, *Nano Lett.* **2019**, *19*, 29.

[22] R. He, G. Tian, S. Li, Z. Han, W. Zhong, S. Cheng, J. Xie, *Nano Lett.* **2022**, *22*, 2429.

[23] J. Li, C. Lin, M. Weng, Y. Qiu, P. Chen, K. Yang, W. Huang, Y. Hong, J. Li, M. Zhang, C. Dong, W. Zhao, Z. Xu, X. Wang, K. Xu, J. Sun, F. Pan, *Nat. Nanotechnol.* **2021**, *16*, 599.

[24] L. Wang, T. Liu, T. Wu, J. Lu, *Nature* **2022**, *611*, 61.

[25] S. Li, G. Tian, R. Xiong, R. He, S. Chen, H. Zhou, Y. Wu, Z. Han, C. Yu, S. Cheng, J. Xie, *Energy Storage Mater.* **2022**, *46*, 443.

[26] T. Liu, J. Liu, L. Li, L. Yu, J. Diao, T. Zhou, S. Li, A. Dai, W. Zhao, S. Xu, Y. Ren, L. Wang, T. Wu, R. Qi, Y. Xiao, J. Zheng, W. Cha, R. Harder, I. Robinson, J. Wen, J. Lu, F. Pan, K. Amine, *Nature* **2022**, *606*, 305.

[27] C. Xu, K. Marker, J. Lee, A. Mahadevegowda, P. J. Reeves, S. J. Day, M. F. Groh, S. P. Emge, C. Ducati, B. Layla Mehdi, C. C. Tang, C. P. Grey, *Nat. Mater.* **2021**, *20*, 84.

[28] F. Lin, I. M. Markus, D. Nordlund, T. C. Weng, M. D. Asta, H. L. Xin, M. M. Doeff, *Nat. Commun.* **2014**, *5*, 3529.

[29] C. Lin, J. Li, Z. W. Yin, W. Huang, Q. Zhao, Q. Weng, Q. Liu, J. Sun, G. Chen, F. Pan, *Adv. Mater.* **2023**, *36*, 2307404.

[30] M. D. Radin, S. Hy, M. Sina, C. C. Fang, H. D. Liu, J. Vinckeviciute, M. H. Zhang, M. S. Whittingham, Y. S. Meng, A. Van der Ven, *Adv. Energy Mater.* **2017**, *7*, 1602888.

[31] J. Lee, D. A. Kitchaev, D. H. Kwon, C. W. Lee, J. K. Papp, Y. S. Liu, Z. Lun, R. J. Clement, T. Shi, B. D. McCloskey, J. Guo, M. Balasubramanian, G. Ceder, *Nature* **2018**, *556*, 185.

[32] Z. Lun, B. Ouyang, D. A. Kitchaev, R. J. Clément, J. K. Papp, M. Balasubramanian, Y. Tian, T. Lei, T. Shi, B. D. McCloskey, J. Lee, G. Ceder, *Adv. Energy Mater.* **2018**, *9*, 1802959.

[33] J. Qian, Y. Ha, K. P. Koirala, D. Huang, Z. Huang, V. S. Battaglia, C. Wang, W. Yang, W. Tong, *Adv. Funct. Mater.* **2023**, *33*, 2205972.

[34] E. Hu, Q. Li, X. Wang, F. Meng, J. Liu, J.-N. Zhang, K. Page, W. Xu, L. Gu, R. Xiao, H. Li, X. Huang, L. Chen, W. Yang, X. Yu, X.-Q. Yang, *Joule* **2021**, *5*, 720.

[35] W. S. Yoon, K. B. Kim, M. G. Kim, M. K. Lee, H. J. Shin, J. M. Lee, J. S. Lee, C. H. Yo, *J. Phys. Chem. B* **2002**, *106*, 2526.

[36] J. Rodriguez-Carvajal, *Phys. B* **1993**, *192*, 55.

[37] S. R. Stock, D. Gürsoy, F. De Carlo, X. Xiao, C. Jacobsen, Proc. SPIE 9212, Developments in X-Ray Tomography IX **2014**, 9120N.

[38] M. Ge, W. K. Lee, *J. Synchrotron Rad.* **2020**, *27*, 567.

[39] E. Nazaretski, H. Yan, K. Lauer, N. Bouet, X. Huang, W. Xu, J. Zhou, D. Shu, Y. Hwu, Y. S. Chu, *J. Synchrotron Rad.* **2017**, *24*, 1113.

[40] G. Kresse, J. Hafner, *Phys. Rev. B* **1993**, *47*, 558.

[41] G. Kresse, J. Furthmuller, *Phys. Rev. B* **1996**, *54*, 11169.

[42] S. K. Mishra, G. Ceder, *Phys. Rev. B* **1999**, *59*, 6120.

[43] G. Kresse, J. Furthmiiller, *Comp. Mater. Sci.* **1996**, *6*, 15.

[44] A. Jain, G. Hautier, S. P. Ong, C. J. Moore, C. C. Fischer, K. A. Persson, G. Ceder, *Phys. Rev. B* **2011**, *84*, 045115.

[45] S. Grimme, J. Antony, S. Ehrlich, H. Krieg, *J. Chem. Phys.* **2010**, *132*, 154104.